DETECTION AND CHARACTERIZATION OF ROLLING CONTACT FATIGUE TYPES OF DEFECTS USING SURFACE ACOUSTIC WAVES

By

Alex Tian Vu

A THESIS

Submitted to
Michigan State University
in partial fulfillment of the requirements
for the degree of

Mechanical Engineering - Master of Science

2022

ABSTRACT

Rolling Contact Fatigue or Damage (RCF/RCD) is the surface and near-surface damage that occurs on the rail head and wheel treads of rail cars. The damage in the rail head due to progressive cyclic loading from the contact between the wheel and the rail head can lead to formations of small cracks that can ultimately grow and join up to form a flake that falls loose, leaving behind a cavity in the running surface of the rail or turn downward to a limited depth forming a fatigue crack commonly referred to as head checks and gauge corner cracks. Quantifying RCF/RCD crack depths and density in rails is important for all the railroad authority and industries to manage their grinding programs effectively and efficiently. Detecting RCF/RCD can be challenging due to the size of the cracks, which typically starts out at $2 - 10\mu m$ and progressively can grow up to depths of $3mm$ to $5mm$. It becomes impossible to characterize these early stage RCF cracks without physically destroying the sample to get to the area of interest. To gain a better understanding, the cracks that are formed from RCF/RCD can be simplified into four different types: (I) vertical/normal, (II) oblique, (III) branched, and (IV) clustered cracks. Methods that can accurately detect and characterize these cracks non-destructively have been of high interest for the rail community.

This work focuses on utilizing Surface Acoustic Waves (SAWs) for detection and characterization of RCF/RCD defects through numerical simulations the using finite element method (FEM). A transient, elastodynamics wave propagation model was used to simulate SAW propagation. Parameters such as the transmission (Tc), reflection (Rc), scattered (Ps), and time of flight(TOF) were extracted from the model and quantified to build relationships for understanding the mode conversion and interaction phenomena. The different type of defects that were modeled in FE included vertical, oblique, and branched defects. First, SAW interaction with a set of vertical, oblique and branched RCF defects were studied by quantifying Tc. The Tc values exhibit duality at certain crack angles, which makes it challenging to accurately characterize oblique RCF/RCD type of defects. Experiments have been done to validate vertical and oblique defects: the results also exhibit a duality in Tc for the oblique defects. To understand branched crack morphology, the complex crack geometry can be simplified into a series of varying angled elastic wedges, which is part of a classical problem within elastodynamics. Finally, SAW interaction with clustered cracks for two sets of densely packed RCF/RCD type of defects: a uniform cluster and a non-uniform cluster to further develop characterization techniques using Tc/Rc relationships and through signal processing methods.

The impact of this work is to provide a proof of concept that the presented numerical results can be validated through experiments and become field implemented.

This work will be dedicated to my family for all the support they have given me throughout my entire academic career here at MSU. To both of my mothers and my dad for giving me the moral support for whenever I was stressed with my work. To my grandparents for giving me some tips for this whole process, since they have both been through it once before. To my three dogs, that gave me something to look forward to see at the end of each week. And to all my friends, old and new, that I have met along the way.

ACKNOWLEDGEMENTS

I would like to give a special thanks to my following professors and colleagues:

To my thesis advisor Dr. Sunil K. Chakrapani for his contribution to my thesis work for the past 1.5 years. For his contribution in works submitted to the Journal for Research in Nondestructive Evaluation(RNDE) and the Journal of the Acoustical Society of America(JASA).

To my committee members Dr. Lalita Udpa and Dr. Siva Nadimpalli for taking the time to oversee my final defense.

To Dr. Anish Poudel for his support from MxV rail (formerly known as Transportation Technology Center, Inc.) under the Association of American Railroads (AAR) sponsored strategic research initiative (SRI) university programs, with work submitted to the Journal for Research in Nondestructive Evaluation(RNDE).

To Yoganandh Maduranthakam with work submitted to the Journal for Research in Nondestructive Evaluation(RNDE).

To the Physical Ultrasonics, Microscopy and Acoustics (PUMA) Lab for providing the resources to conduct my experiments.

To Professor Katherine Stevenson, for giving me the opportunity to become an instructor for an undergraduate course ME280 alongside her. This provided an outlet for me to shift focus at times, so that I would not become fully engulfed in solely research.

To Professor Craig Gunn, for proof-reading my thesis and providing feedback.

TABLE OF CONTENTS

Chapter 1

INTRODUCTION

1.1 Rolling Contact Fatigue/Damage

RCF/RCD is the surface and near-surface damage that occurs on the rail head and wheel treads of rail cars. It encompasses ductility exhaustion, cracking, and material flow, as well as near-surface cracks and material fatigue in the layers below the surface[1, 2]. RCF/RCD in the rail is primarily a result of the wheel-rail interaction. The damage in the rail head due to progressive cyclic loading from the contact between the wheel and the rail head can lead to the formations of small cracks that can ultimately grow and join up to form a flake that falls loose, leaving behind a cavity in the running surface of the rail or turn downward to a limited depth forming a fatigue crack commonly referred to as head checks and gauge corner cracks. The onset of RCF/RCD and its propagation mechanism are governed by the contact stresses, traction forces on rails along with shear stresses and residual stresses evolved from asymmetric load-unload pattern giving rise to plastic strain accumulation[3, 4], which continually gets more severe with more load cycles. Head checks, gauge-corner cracks, flaking, squats, spalling, and shelling are all names for surface or near-surface initiated RCF/RCD in railroad rails[5, 6]. RCF/RCD has been at the forefront of railroad research for years, and accurate in-motion non-contact Nondestructive Evaluation(NDE) methods of defect characterization remain a challenge to be discovered[5, 6]. Fig. 1.1,a-c shows simpler cases of RCF/RCD crack configurations in the rail head. A simplified crack progression model for the various stages of RCF/RCD propagation from crack initiation to full rail-break was used by Kapoor et al[7] for easier visualization of RCF/RCD defects. Fig. 1.2,a and b shows two different cases of RCF/RCD cracks that can form in the rail head in a cluster configuration. Detecting RCF/RCD can be challenging due to the size of the cracks, which typically starts out at $2 - 10\mu m$ and progressively can grow to depths of $3mm$ to $5mm$[5, 6, 8–11]. At the early stage, due to the relatively small size of the cracks, the sensitivity can be poor due to numerous additional variables such as operating temperature, contamination, and harsh railroad environment[5, 12]. Due to these challenges, some of the existing NDE techniques explored or developed have shown limited success to effectively detect and characterize RCF/RCD cracks in the rail head. Failure to accurately characterize RCF/RCD crack depth can cause other severe underlying issues, which is of critical importance to the rail safety[5, 6, 13, 14].

A traditional UT approach has been used for inspecting rails for internal deep fatigue defects[15–18]. This includes roller search units (RSUs) equipped with ultrasonic probes that can roll over the track and maintain contact, which makes it field implementable. Traditional

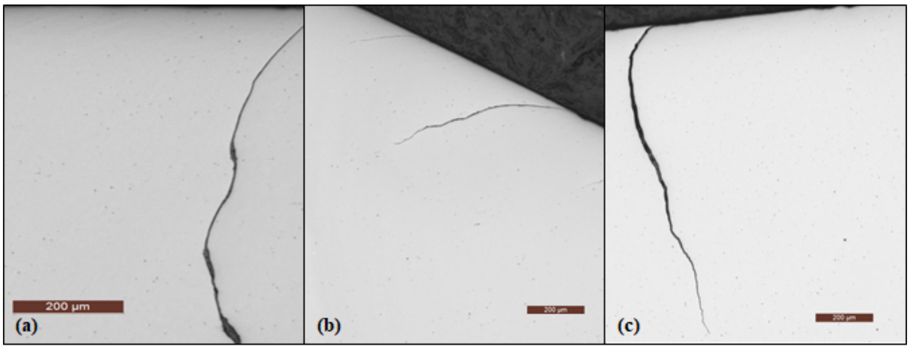

Figure 1.1: Micrograph images of 3 surface breaking cracks (These micrographs, were provided by Dr. Anish from MxV Rail).

UT cannot be used for characterizing surface or near surface cracks due to physical limitations. Therefore, surface breaking defects in the rail head have traditionally been detected and characterized using electromagnetic NDE methods, primarily Eddy Current Testing (ET)[12, 19, 20]. ET is fully non-contact, which makes it desirable for in-motion field implementation; however, RCF/RCD crack depth cannot be measured accurately, and it has limited depth sensitivity [12, 17, 19–23]. Recently, research lead by MxV rail is investigating the use of electromagnetic field imaging (EMFI) technology for RCF/RCD crack depth characterization[1, 2, 10, 11].

However, for surface breaking defects Rayleigh wave NDE can offer alternatives to defect characterization due to localized wave propagation[24]. Rayleigh waves are surface propagating waves that satisfy a stress-free boundary condition along the surface of a half-space, with the acoustic energy typically being confined to 1.5 times the wavelength. This makes them advantageous in UT NDE of surface and sub-surface features [24–27]. RCF/RCD defects typically tend to form as oblique and branched cracks rather than straight cracks. While there are several research articles that have explored Rayleigh wave interaction with vertical surface breaking defects, research on oblique cracks in a wide range of angles is limited [28, 29] and research on branched cracks where it continues down through the rail has not yet been explored. There are a few articles that have explored branch cracks from a stress corrosion cracking(SCC) process, where the crack can start out as a vertical slot and can either branch from the top or the center of the vertical slot[29, 30]. But, these are fundamentally different from RCF/RCD defects in the rail head.

The objective of this work is to understand how Rayleigh waves can be used for detection and characterization of RCF/RCD in the rail head. Therefore, it is necessary to understand their interactions with the four different types: (I) vertical/normal, (II) oblique, (III) branched, and (IV) clustered cracks of RCF/RCD defects and the expected response. By building a set of calibration curves, we envision eventually applying these directly to determine the crack morphology such as length, orientation, and the overall severity of the crack. This work utilizes

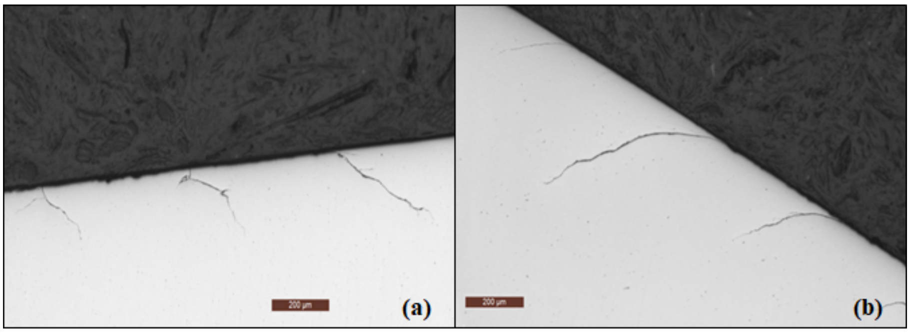

Figure 1.2: Micrograph images of 2 different sets of surface breaking cluster cracks (These micrographs, were provided by Dr. Anish from MxV Rail).

FEM to study the interaction of Rayleigh wave with surface breaking, vertical, oblique, and branch defects. Further, to understand the response from real cracks, the crack morphology was modeled from a micrograph and wave propagation simulation was carried out. This emphasizes the challenges when characterizing real cracks with curvilinear profile and rough surfaces. The numerical approach allows us to fully understand the Rayleigh wave response and help with experimental design to detect these complex defects in the field.

1.2 Elastic Wedge

In order to understand the complex morphology of branched RCF/RCD type of defects, they can be simplified into a series of varying angled elastic wedges as observed in Fig. 1.3.

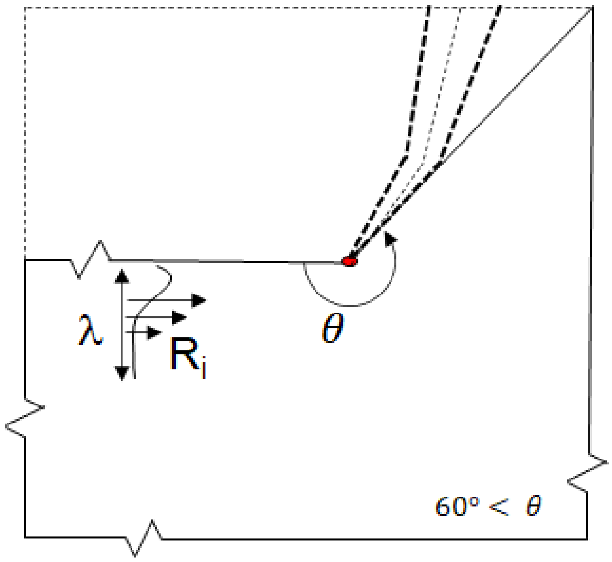

Figure 1.3: Schematic of simplification of branched crack to elastic wedge.

Surface or Rayleigh wave interaction with an elastic wedge is one of the more interesting and unsolved classical problems in the area of geophysics and acoustics[31–35]. Rayleigh surface waves can propagate only along the stress-free boundary of a half-space, with their energy confined to the sub-surface and decays exponentially along the thickness [24, 36–39]. Rayleigh wave interaction with discontinuities can produce mode conversions, that will result in transmission, scattering, and reflection. Rayleigh wave interaction with discontinuity has been of significant interest to several communities including geophysics, acoustics, and nondestructive evaluation [24, 33, 40–42]. Raleigh wave propagation and interaction with a wedge like discontinuity can be simplified as two ends of an elastic boundary that meet at a non-orthogonal angle while satisfying stress-free boundary conditions. This approach has been used in geophysics to simplify the complex topography caused by mountains and other landmarks in geophysics[33, 40]. These studies provide a gateway to understanding the Rayleigh wave scattering on a seismic scale by analysis via analytical or numerical methods. Many researchers such as A.K. Mal[31, 33], L. Knopoff[31–34], A.F. Gangi[34, 35], A.K. Gautesen[43–47], and more[41, 48–50] have studied the mode conversion, transmission, reflection, and scattering phenomena in an elastic wedge. An incident Rayleigh wave mode converts into bulk modes upon interacting with the discontinuity. Both transmission and reflection coefficients for Rayleigh wave interaction with a step-change and at a corner has been reported by A.K. Mal[31, 33]. These types of wedges can be similar to a 90° or a 270° wedge. The transmission and reflection coefficients for Rayleigh wave interaction with a varying angled wedge has also been observed experimentally by A.K. Mal[33], L. Knopoff[33, 34], and A.F. Gangi[34, 35].

The numerical models used in this work were based on Gautesen's analytical models[43–47] using a set of Green's function integrals to capture the Tc, Rc(will be referred to as "coefficients" afterwards), and their respective phase at a Poisson's ratio of $v = 1/3$ and $v = 1/4$ for a wedge angle range of 63° to 350°. Gautesen observed many fluctuations for the coefficients at angles $\theta < 180°$, while Tc reduces in value, Rc experiences a small increase for wedge angles $\theta > 180°$. A.K. Mal and L. Knopoff[31–33] also used a set of Green's function integrals derived from Huygens' principle to capture the displacements for the reflected and transmitted waves. This approach seems to reduce the error between the analytical and experimental results. Other researchers, such as K. Fuji et al[48, 49], had proposed wedge models using sets of complex integrals and that the coefficients experienced high fluctuations from a wedge angle of 36° to 180°. B.V. Budaev et al[41] has proposed Sommerfeld's integrals to capture the transmitted, reflected, and scattered energy. The experimental coefficients at small wedge angles less than or equal to 90° exhibited considerable error; thus, they only considered wedge angles greater than 95°. One of the challenges in using analytical models is being able to calculate the coefficients effectively when the wedge angle would become very small such that it would produce many irrelevant reflected waves[31, 33, 41, 43, 44] thus complicating the resulting coefficients. Another challenge with classical analytical models is that the scattering phenomena may not be fully captured. Rayleigh wave interaction with discontinuities can result in a wide range of mode conversions and different incident waves on the half-space boundary. This can be more complicated for the case of an acute wedge, where multiple overlapping internal reflections can cause mode conversions and constructive and destructive interference. Therefore, revisiting the interaction for the acute angles using powerful numerical solvers can be beneficial to our understanding of the classical wedge problem.

While the previous research in literature have studied several different structures and geometries, they have not studied the effect of frequency. Changing the excitation frequency will change the wavelength of the incident wave, which may change interaction phenomenon, primarily due to the amount of out-of-plane energy that interacts with the discontinuity. This might have little effect on wedge angles $\theta > 180°$ shown in Fig. 2.5,b, since the 2nd stress-free edges of the wedge is beyond the incident energy. But for wedge angles $\theta < 180°$ shown in Fig. 2.5,a, the incident wavelength may have a larger effect, especially since the two stress-free edges wedge converge as shown in Fig. 2.5,a[31, 33, 41, 43, 44]. We can hypothesize that the incident wavelength will have an effect on the interactions especially for wedge angles $\theta < 180°$. The change in wavelength may also affect the phase of the transmitted wave. As the wedge angle reduces to $< 90°$, superposition and multiple interactions of waves can affect the phase of the transmitted waves. The primary source of reflection, transmission, and scattering of an incident Rayleigh wave is the discontinuity (D1 as shown in Fig. 5.3,a-b). Rayleigh wave interaction with D1 can change if the geometry of D1 changes, i.e, going from a sharp transition to a smooth/continuous transition. Many researchers[41, 43–50] have studied similar problems analytically. A.F. Gangi[40], H. Wong[35], and F.J. Sanchez-Sesma et al[51] have also explored the effects of various mode conversion phenomena in a changing semi-elliptical geometry.

The objective of this work is to revisit Gautesen's models[43–47] using numerical simulations to understand the limitations and gain a deeper understanding of the classical wedge problem. In order to understand the mode conversion phenomena, a relationship between the transmission, reflection, and scattered coefficients as a function of wedge angle for changing excitation frequencies and will be presented in Sect. 5.1. Understanding the effect of changing the excitation frequency is very important to this work, such that it will provide insight on its dependence for mode conversion, interaction, coefficients, and phase. From this idea, a hypothesis was formed and will be discussed in Sect. 5.1. The same hypothesis was applied to the effect on the phase and transition geometry type at each wedge angle, which will be discussed in Sects. 5.2 - 5.3.

Chapter 2

NUMERICAL MODEL

2.1 Numerical Setup

Numerical simulations were carried out using ANSYS, which allows us to capture phenomena like mode conversion, interaction, transmission, reflection, and scattered coefficients. A rectangular two-dimensional (2D) model with different types of cracks and varying angled wedges were created using simple Boolean operations as observed in Fig. 2.3, 2.4 and in Fig. 2.5,a-b respectively. All the surfaces and boundaries for each model and including the inside of the cracks were attributed with stress-free properties.

Each model was sufficiently large to ensure reflections from the boundaries do not interfere with the incident and scattered wave packets within the prescribed time. The models were meshed with 8 noded quadrilateral elements with quadratic shape functions to satisfy the convergence criteria of 10 elements per λ[25, 52, 53], and the total solve time and time step was varied to satisfy the Nyquist criteria. A meshed area at the crack can be found in Fig. 2.1,a. When the excitation frequency changes, the model was re-meshed to re-satisfy the convergence and Nyquist criteria. Standard steel isotropic material properties were assigned to a 2D model and are as follows: $\nu = 0.3, E = 210GPa, \rho = 7850kg/m^3$. The objective of the 2D plane strain approximation is to focus on understanding the interaction and mode conversion phenomenon.

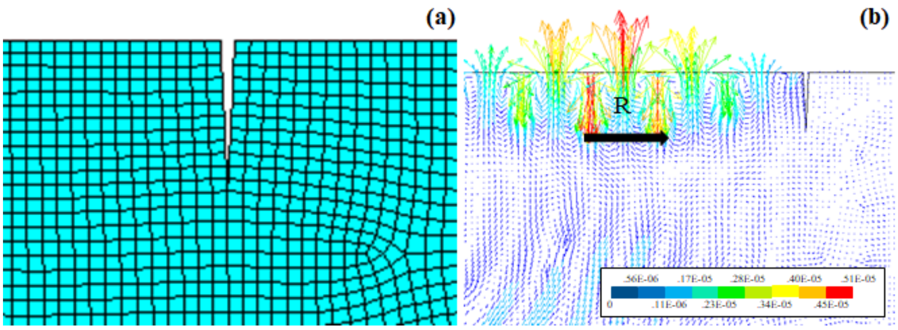

Figure 2.1: (a) Example meshed area of a vertical crack. (b) Vector plot of incident Rayleigh wave before interaction.

A transient analysis was carried out with an initial input of 1 MHz, 7 cycle tone-burst[25, 54] with a total simulation time of $50\mu s$ and $50ns$ time step. Newmark's time integration scheme was used for time stepping, and the direct sparse solver was used to solve the problem. Once the model is solved, at each node, the temporal profile of the displacement components were extracted to measure the coefficients.

The source was modeled on the horizontal boundary at a distance away from the start of the crack shown in Figs. 2.3, 2.4 and D1 shown in Fig. 2.5 such that a single reflected wave packet of Rayleigh wave could be extracted. The position of the receiver was selected based on shape of the transmitted wave packet, i.e. a complete wave packet without any additional overlapping waves. The y-displacement A-Scan is shown in Fig. 2.2,a and b where, A_i, A_r and A_t are the incident, received and transmitted amplitudes. The acoustic power of the Rayleigh wave is given by Eq. (2.1)[55]:

$$P = \frac{1}{t}\int_0^t \int^{D_i} (\sigma_{xx}\dot{u} + \sigma_{xy}\dot{v})\, dydt \tag{2.1}$$

For Rayleigh waves, the integration must be carried out over the section D_i, which corresponds to $1.5 \times \lambda$. σ_{xx} and σ_{xy} are the axial stress and in-plane shear stresses, and $\dot{u}$ and $\dot{v}$ are the in-plane velocities. The transmission (Tc) and reflection (Rc) coefficients can be directly calculated using the acoustic power: $T_c = P_t/P_i$, and $R_c = P_r/P_i$. The scattering coefficient P_s (included in reference as "coefficients" with Tc and Rc) can be obtained using the power flux balance: $T_c + R_c + P_s = 1$. Since the incident, transmitted and reflected modes are Rayleigh waves; the transmission and reflection coefficients can also be calculated by using simpler definition: $T_c = A_t/A_i$, and $R_c = A_r/A_i$ [28, 56], which was used in the work. A validation was also performed to ensure that both definitions produce the same value of transmission and reflection coefficient.

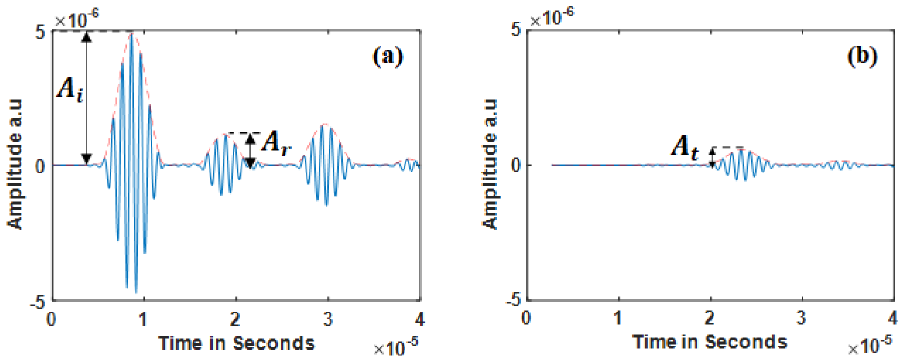

Figure 2.2: Numerical A-Scans showing (a) Uy amplitude displacement for incident and reflection. (b) Uy amplitude displacement for transmission.

2.2 RCF Setup

2.2.1 Single defects

This work extends previously presented numerical results at a conference [57]. For all cracks shown in Fig. 2.3 the parameters will be as followed. For the vertical cracks, the width w being kept at a 1:2 ratio to the depth, and depth A varied from 0 to 3mm. For the oblique cracks, the depth B ranged from 0.5 to 3mm with the width w being kept at a 1:2 ratio to the depth, and the angle θ was swept from $-70°$ to $70°$ measured from the vertical. Branched cracks can be considered as a continuation of obliques, in a sense that the first section was kept at a constant depth h of 1mm and an incident angle θ_1 of 25° [5, 6, 8]. The second section begins at the end of the former by varying the length L from 1 to 5mm and the angle θ_2 from 0° to $-80°$ clockwise (CW) measured from the vertical.

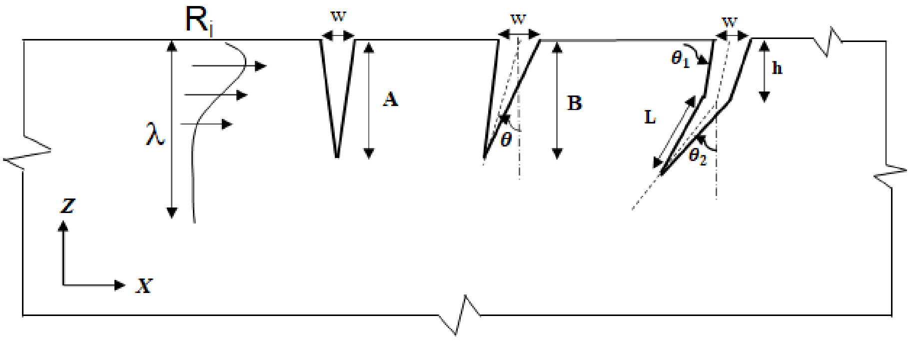

Figure 2.3: Schematic of Cracks: vertical, oblique and branched.

2.2.2 Uniform cluster defects

To determine some parameters when creating the model for the uniform cluster defects, approximations were taken from the micrographs shown in Fig. 1.2,a and b. It was determined that the average spacing between each defect was $\approx 500\mu m$. The depths of each defect came to be $\approx 200\mu m$ to $400\mu m$. The oblique angle θ measured from the vertical, was determined to be $\approx 45°$ to $65°$.

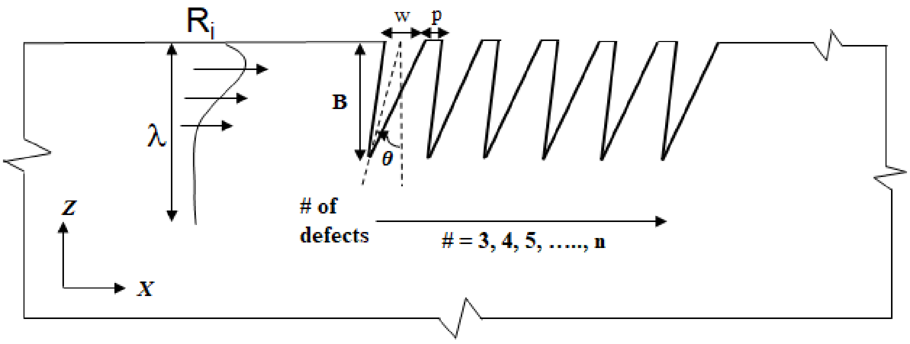

Figure 2.4: Schematic of uniform cluster cracks.

Using these approximations taken from the micrographs, they were applied to the uniform clusters by modeling a single oblique defect and then adding an exact copy to the right of the first defect depending on the number in a given cluster as shown in Fig. 2.4. The width w, the pitch p and the oblique angle θ were kept constant at $10\mu m$, $500\mu m$ and 45° respectively. The number of defects in a cluster varied from 3 - 7 cracks. The depth of the defect B was varied from $200\mu m$ - $1000\mu m$ at increments of $100\mu m$.

2.3 Wedge Setup

The wedge was created by fixing the top/inner horizontal boundary in place and sweeping the inner angled boundary by an angle θ at the wedge point vertex from 60° to 350° as shown in Fig. 2.5,a-b. Where 330° to 350° wedges mimic a horizontal semi-infinite crack and have been previously reported by Chakrapani[25].

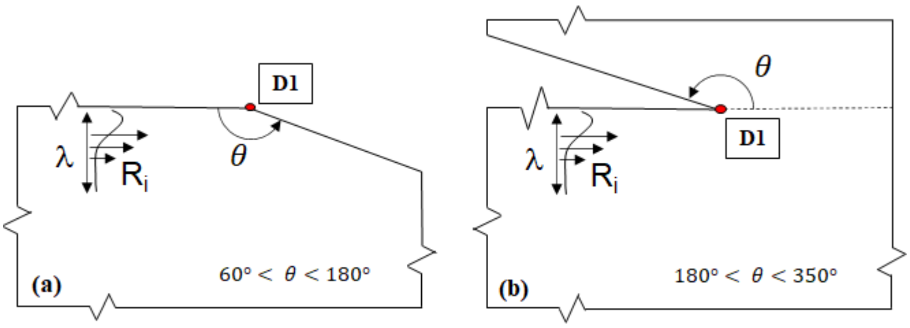

Figure 2.5: Schematic of wedge for angles (a) 60° to 180°. (b) 180° to 350°.

Chapter 3

RAYLEIGH WAVE INTERACTION WITH RCF TYPE OF DEFECTS

This chapter will focus on the numerical analysis of surface wave interaction with RCF type of defects. The following results presented in this chapter were part of a collaborative effort submitted to the Journal of Research in Nondestructive Evaluation(RNDE).

3.1 Vertical Defects

The Tc vs Normalized Depth plot is shown in Fig. 3.1. The crack depth has been normalized to the wavelength to generalize the results. From this plot, it can be seen that the Tc value becomes asymptotic at $\approx 19\%$ when the defect is at a normalized depth value of 0.67. The Tc then experiences a 2% fluctuation beyond a normalized value of 0.67. In general, the results agree with the idea of Tc being inversely proportional to defect depth. An additional study on the effect of changing crack width on the Tc response was done at a 3mm crack depth and a crack width ranging from 0.1mm to 1.1mm shown in Fig. 3.8.

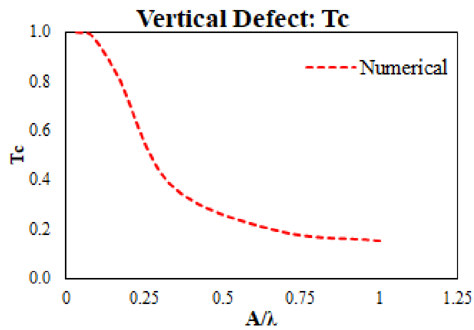

Figure 3.1: Vertical Defect: Tc vs Depth normalized to wavelength.

3.2 Oblique Defects

The variation of Tc as a function of the crack orientation is shown in Fig. 3.2,a-d for different crack depths. As can be observed in Fig. 3.2,b , the Tc as a function of crack orientation exhibits a sinusoidal variation. Furthermore, these are symmetric between the -ve and +ve oblique angles. But both the symmetry and sinusoidal variation seem to disappear as the crack depth increases. Furthermore, due to the combined effects of symmetry and sinusoidal behavior, a duality in the value of Tc can be observed, i.e, both $0°$ and $-60°$ cracks exhibit the same Tc values. This makes it challenging to describe a simple calibration plot.

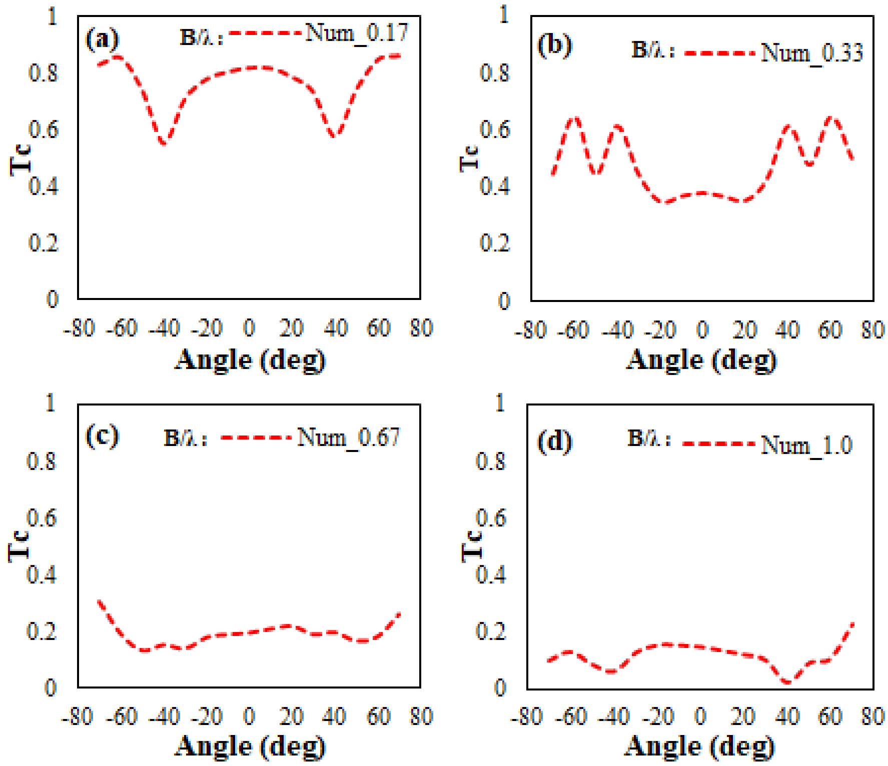

Figure 3.2: Oblique cracks: Tc vs Angle at a normalized depth: (a) 0.17(0.5mm). (b) 0.33(1.0mm). (c) 0.67(2.0mm). (d) 1.0(3.0mm).

3.3 Branch Defects

The branch crack studies involve more parameters such as branch angle (θ_2) and branch length (L). A total of 26 (25 branch combinations and 1 reference) simulations were carried out to expand on all the combinations of θ_2 and L. The Tc values are plotted in Fig. 3.3,a and b in two different ways. Both show a decreasing trend, which is expected as a function of angle and length. For branch angles of $0°, -20°, and - 40°$, they follow the fundamental wave propagation idea as discussed in Sect. 3.1 and Sect. 3.2. However, the $-60°, and - 80°$ angles exhibit a sinusoidal variation with increasing branch length. Once again, this results in a duality of Tc.

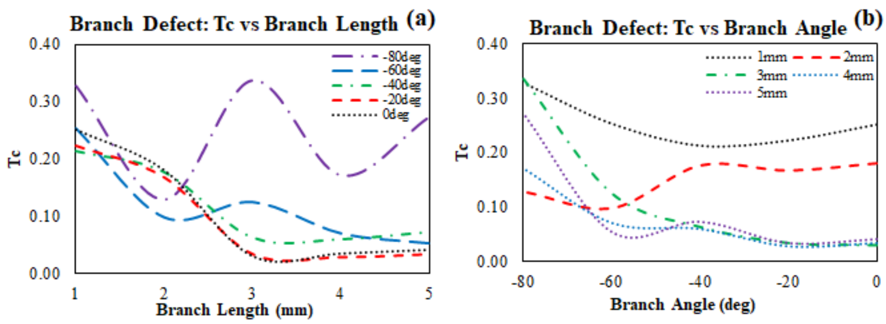

Figure 3.3: Transmission coefficient of branch cracks: (a) Tc vs. Branch angle θ_2 for different branch lengths L. (b) Tc vs. Branch length L for different branch angle θ_2. The same data has been represented in two different forms.

3.4 Cracks from Micro-graphs

The cracks presented in Sect. 2.2 are idealized cracks, which have planar and smooth crack faces. However, real RCF/RCD cracks as shown in Fig. 1.1,a-c have curvilinear profile and rough faces. To test the ideal crack results in Sect. 3.1 - 3.3 and compare them against real cracks, the micrographs were used to model real cracks. The cracks that were picked from the micrographs, were decided so that they would ideally be as close as possible to the numerical models in overall crack depth. Cracks (a) and (c) from Fig. 1.1,a-c averaged $1mm$ in overall crack depth, whereas crack (b) was approximately $500\mu m$.

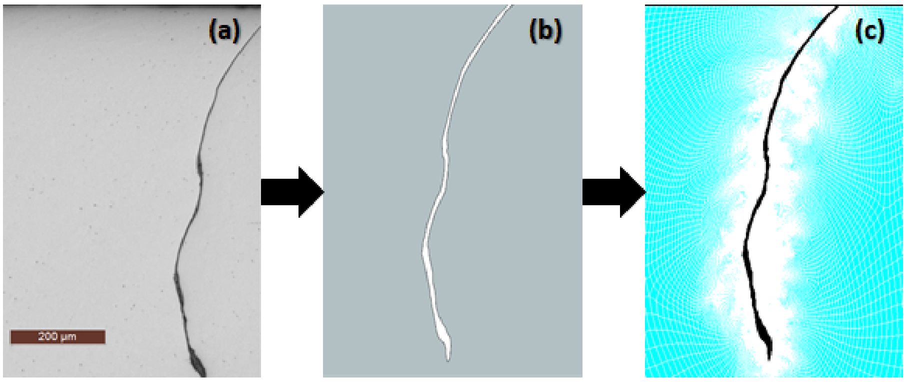

Figure 3.4: Real defect modeling process: (a) Micrograph. (b) 2D CAD model with crack. (c) FE Meshed area of a real crack.

From a given micrograph an initial assumption can be assigned to the defect as to what the geometry can be from the three options: vertical, oblique, or branched. The cracks were then modeled using computer aided design software(CAD) to create the 2D geometry, which was then meshed and a transient analysis was carried out. A schematic of this process is shown in Fig. 3.4,a-c. This process was carried out for the three cracks shown in Fig. 1.1,a-c. The numerical Tc for these cracks are shown in Fig. 3.7. These will be further discussed in Sect. 3.6.

3.5 Uniform Clusters

The uniform clusters involve two varying parameters such as the depth B and the number of defects in the section. In total, 26 simulations were carried out to expand on all quantity and defect depth combinations (25 cluster combinations and 1 reference). The Tc and Rc has been plotted as a function of defect depth for an increasing number of defects shown in Fig. 3.5,a and b. Between 3 - 7 defects, there is no clear distinction in Tc or Rc across any number of defects as they all follow a relatively similar value for all depths. In Fig. 3.5,a and b the Tc and Rc follow a parabolic trend with no separation for a defect depth of $200\mu m$ to about $400\mu m$ and $500\mu m$ for Tc and Rc respectively. Although after the parabolic trend, they then follow an inverse monotonic trend to a defect depth of $1000\mu m$. This is expected for Tc and Rc as a function of defect depth.

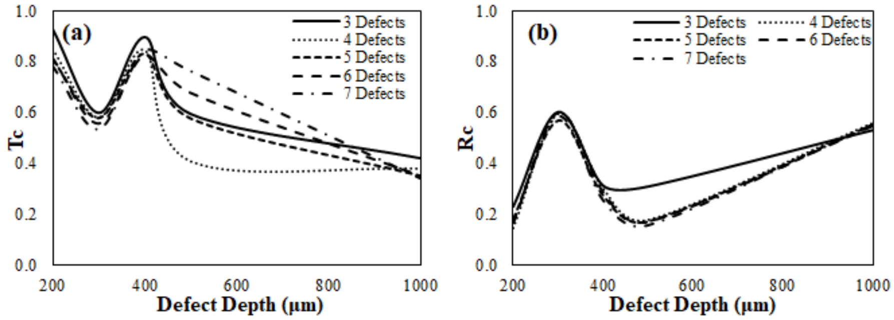

Figure 3.5: Comparing the number of defects in a cluster for (a) Tc vs Defect depth. (b) Rc vs Defect depth.

The data from Fig. 3.5 can also be represented in a different form to show the dependence of Tc and Rc on the number of defects for different defect depths as shown in Fig. 3.6,a and b. It can be observed that for an increasing number of defects in the cluster, the Tc and Rc exhibits an asymptotic response. At a defect depth of $500\mu m$, the Tc does not exhibit a similar asymptotic response for an increasing number of defects as observed in Fig. 3.6,a.

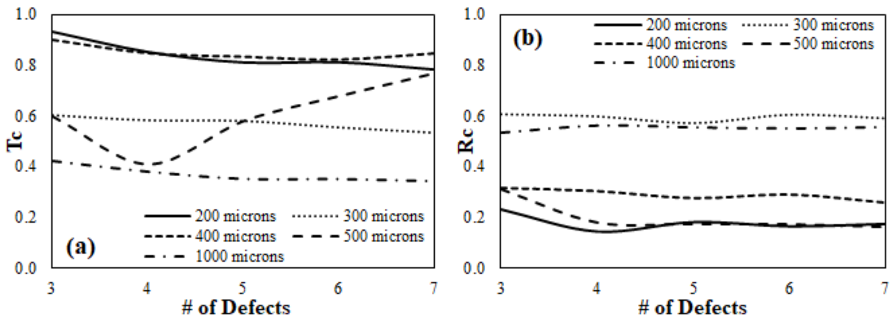

Figure 3.6: Comparing the defect depths in a cluster for (a) Tc vs Number of defects. (b) Rc vs Number of defects.

3.6 Discussion

Effect of crack geometry: The objective of this work is to use the model to capture the physics and trends, which can further be extrapolated to real applications.

Comparing the present results to previously published results[56, 58], there is a good qualitative agreement in terms of trends for all the defects. In certain cases, the absolute values don't match. Compared to other existing models, there are a few differences in the assumptions: (a) this work uses sharp crack tips, whereas most existing work uses slot-like structures, (b) this work assumes a non-constant crack width, whereas existing work uses the same slot width. Several researchers [59–61] have explored the effects of scattering from the crack tip with rectangular geometry or slot-like structures. However, real RCF/RCD cracks will be

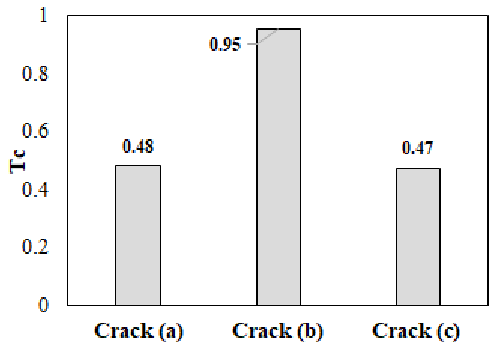

Figure 3.7: Transmission coefficients of three defects from the micrographs with assumed crack geometry: Crack (a) 10deg Oblique. Crack (b) 50deg Oblique. Crack (c) 0deg Branch.

similar to the sharp cracks as seen in the micrographs shown in Fig. 1.1,a-c. A triangular crack has finite width or crack opening, which is important to capture while simulating. Therefore, the numerical models presented here use triangular cracks with sharp crack tips.

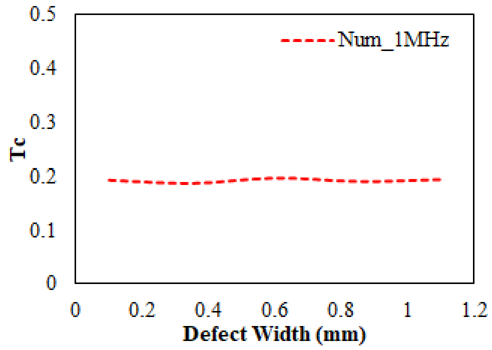

Figure 3.8: Tc vs varying crack width for a vertical triangular defect at a 3mm depth.

To understand the effect of varying crack width on the Tc, numerical analysis was performed to calculate Tc as a function of varying defect width, which can be observed in Fig. 3.8 at a 3mm vertical crack depth. It is observed that by varying the crack width, it does not affect the resulting Tc response using a triangular defect geometry. Several researchers[28, 59–61] have studied the effect of slot width on Tc and reported minimal change. Fig. 3.8 shows the similar trend.

Duality of transmission coefficients: To understand the duality in Tc, it is important to understand the interaction of Rayleigh waves with the different RCF type of defects. Typically, this interaction results in reflection and transmission but also strong scattering into bulk modes. The spatial vector plots showing displacement at specific time step is shown in Fig. 3.9,a-c. The scatter patterns for the oblique and vertical cracks are much simpler compared to the branched crack. Since branch crack morphology is more complicated than the others, the scattering of shear (SV) and longitudinal (P) waves will also be higher, this can be observed in

Fig. 3.9,a-c. The scattered modes can further interact with the transmitted waves thus giving anomalous effects as shown in Fig. 3.3,a and b.

Branch Cracks vs Real Cracks: As stated above in Sect. 1.1, branched cracks where the branched section has propagated down into the rail section have yet to be explored, therefore this analysis was purely used to show the complexity in Tc behavior. The real cracks from micrograph images shown in Fig. 1.1,a-c were approximated to three different categories: crack (a) 10° oblique crack, crack (b) 50° oblique crack, and crack (c) 0° branch crack. Crack (a) and (c) exhibit nearly the same Tc value as shown in Fig. 3.7. Correlating the Tc for crack (a) and (c) (from Fig. 3.7) with the oblique results at $B/\lambda = 0.33$ in Fig. 3.2,b (since this matches closely with the Tc value), we notice that it can exhibit a Tc of a $-60°$ to $-30°$; and due to symmetry, they could also be a 30° to 60° oblique cracks as well. This becomes crucial for crack (c), which is the assumed 0° branch crack, because it can be incorrectly characterized as an oblique defect. Furthermore, if we correlate the Tc for crack (b) (from Fig. 3.7) with the oblique results at $B/\lambda = 0.17$ in Fig. 3.2,a we notice that it could either be a $-70°$ to $-60°$ oblique crack or a 60° to 70° oblique crack because of symmetry. This highlights the challenge of characterizing RCF/RCD defects. This also suggests that the linear cracks assumed in the simulations might not be able to help with characterization. A more data driven approach might be necessary to characterize the RCF/RCD.

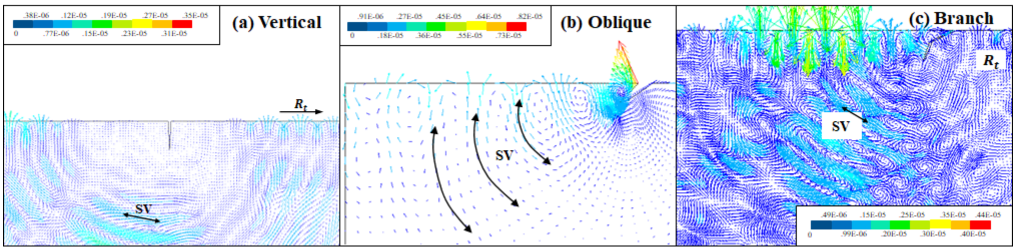

Figure 3.9: Vector plot of scattered waves during defect interaction (a) Vertical. (b) Oblique. (c) Branch.

Effect of number of defects: Understanding a depth dependence on RCF/RCD type of defects has already been researched extensively in the previous sections for a single vertical/normal, oblique, and branched defect. The overall goal of this work is to use the understanding gained from the depth dependence and couple it with the density data to be able to accurately gauge what the relative geometry is for a cluster section.

In the fourth stage of the types of RCF defects that can form along the rail, the complexity in geometry increases with the addition of each defect into the cluster section. A similar trend shown in Fig. 3.6,a and b can also be observed in Fig. 3.1 where the Tc experiences an asymptotic relationship after the defect reaches a normalized depth of 0.67. Combining this understanding along with the duality of Tc experienced with oblique and branched defects, reiterates the fact that a more data driven approach is necessary in order to be able to accurately characterize RCF/RCD type of defects.

Chapter 4

EXPERIMENTAL VALIDATION

The results in this chapter will show experimental validation for the vertical and oblique cracks shown in Chapter 3.

4.1 Experimental Setup

Due to the complex geometry of each type of RCF defect shown in Sect. 2.2 and the current manufacturing limitations, only samples for vertical and oblique cracks were fabricated. The vertical and oblique cracks were fabricated on a rectangular steel plate 3" wide and 1/2" thick. Three defects on both sides of the plate were placed 3" apart to give sufficient space for the transducers to be able to test one defect at a time. Surface grinding was used to create the vertical cracks and the oblique defects were fabricated via wire Electrical Discharge Machining(EDM). For the vertical sample, a 2:1 ratio was kept between depth and width of the defect. For the oblique sample, a $350\mu m$ diameter wire was used to create the six different oblique slots. The physical cracks for vertical defects have sharps crack tips, which is also captured in the models. However, for oblique cracks, sharp crack tips could not be fabricated as the wire EDM results in small slots. But the sharp crack tips of the oblique and branched cracks were captured in the numerical models.

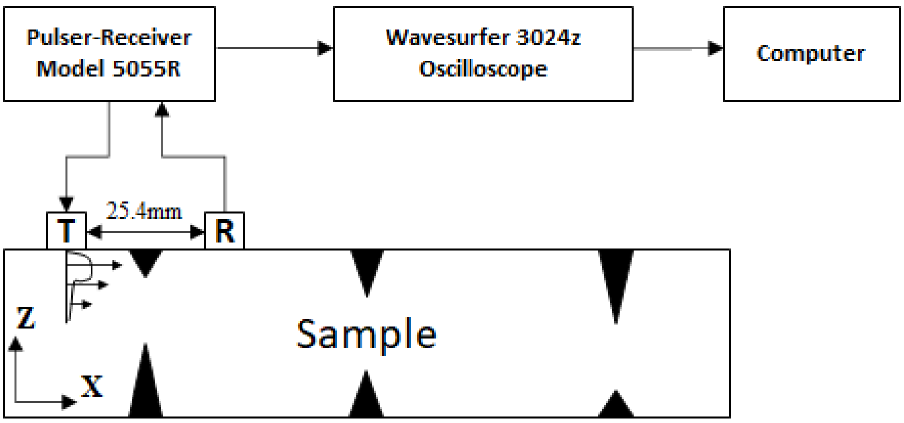

Figure 4.1: Schematic of experimental setup with defect sample, oscilloscope, and waveform generator.

A pair of $1MHz$ contact transducers were placed in a pitch-catch configuration at an angle relative to the surface of the sample for Rayleigh wave generation. The pair of transducers were connected to a Panametrics Pulser-Receiver Model 5055R for creation of the forcing and sync signals. A simple fixture was used to maintain constant separation of $25.4mm$ between the transducers. This electrical signal was then directed to the wavesurfer 3024z Oscilloscope for conversion to digital form. A full schematic of the experimental setup can be found in Fig. 4.1. For quality data acquisition between the transducers and steel sample, couplant glycerin

B was used to ensure a non-porous connection. It is important to note that when setting the oscilloscope, to not change the trigger voltage threshold and to keep the seconds per division constant. Since the cracks extend along the Y-axis, a total of 5 measurements were captured at different spatial positions and the amplitudes were averaged as shown in Fig. 4.2,b and c. The Tc was calculated using the same equation used in Sect. 2.1. The incident amplitude was measured by placing the T-R pair on a sample without any defects at the same spacing as observed in Fig. 4.2,a. The P/R and oscilloscope settings were not changed between the different measurements. This allows us to compare the experimentally measured coefficients.

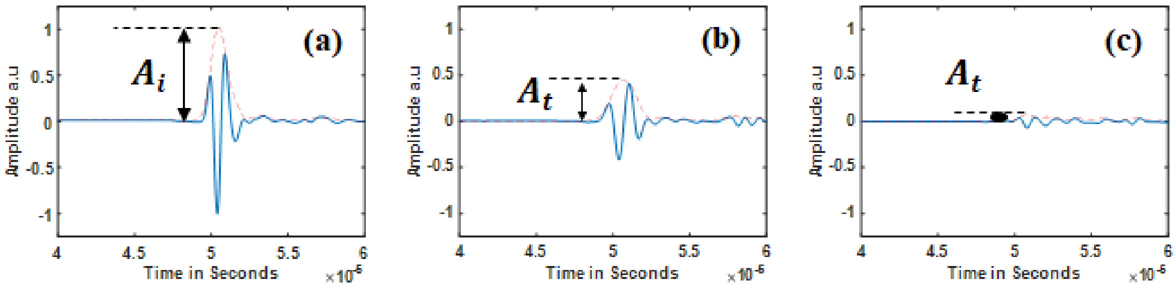

Figure 4.2: Experimental A-Scans showing Uy amplitude displacement for: (a) Reference. (b) 1mm depth. (c) 3mm depth.

4.2 Vertical Defects

The numerical results observed in Fig. 3.1, has been overlaid with the experimental results for vertical defects and shown in Fig. 4.3. By doing a similar post-processing analysis on the steel vertical sample that was fabricated via surface grinding, through experiments a similar asymptotic transmission coefficient trend was captured.

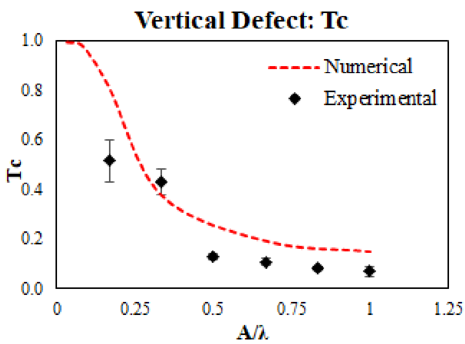

Figure 4.3: Transmission coefficient for vertical cracks. The dashed line is numerical results and the solid diamonds are experimental results. The error bars are also shown for the experimental measurements.

4.3 Oblique Defects

The numerical results observed in Fig. 3.2,b and d, has been overlaid with the experimental results for oblique defects and shown in Fig. 4.4,a and b. Recall that for oblique defects, the numerical results in Fig. 3.2,a-d display both a duality and sinusoidal effects for Tc. Applying the same post-processing analysis as the vertical experiments, the oblique results show a duality in Tc, but does not exhibit the sinusoidal effects shown previously.

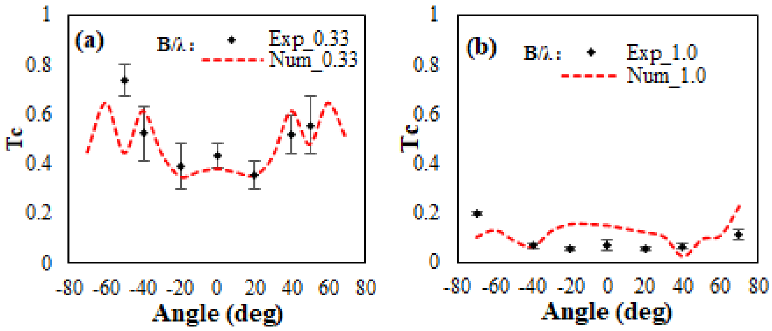

Figure 4.4: Oblique Defects: Tc vs Angle at a normalized depth: (a) 0.33(1.0mm). (b) 1.0(3.0mm). The dashed line is numerical results and the solid diamonds are experimental results. The error bars are also shown for the experimental measurements.

4.4 Discussion

Although, it is possible to create a vertical defect with a triangular geometry through surface grinding. It will result in a rounded crack tip and not the desired sharp crack tip similar to real RCF cracks. When comparing between the numerical and experimental results for the vertical cracks, it can be observed that a similar asymptotic trend occurs at a normalized depth value of 0.67 shown in Fig. 4.3. It was also observed that the absolute experimental values do not match up exactly with its numerical counterpart, where the difference can be attributed to the change in crack tip geometry of a rounded edge to a sharp edge.

As stated in Sect. 4.1 a limitation of the oblique sample is the presence of a flat crack tip as opposed to a sharp crack tip. Another limitation was the ability to create a triangular geometry compared to a slot via wire EDM. It is important to note that from a surface breaking RCF perspective, it is not possible to model real RCF defects without slicing the rail sample nor do RCF defects rarely form with a flat crack tip geometry. Based on the following two limitations, as observed in Fig. 4.4,a and b the experimental results experience changes in overall trend compared to the numerical results. Due to the wire EDM limitations, the width of crack and crack tip is not made exactly as the numerical models. To understand the effect of width on Tc, a numerical analysis was performed and discussed in Sect. 3.6, where it is was observed that the change in width is not a significant contributor to the overall Tc. The major difference between numerical and experimental Tc in Fig. 4.4,a and b is caused by the crack tip geometry.

Chapter 5

RAYLEIGH WAVE INTERACTION WITH AN ELASTIC WEDGE

The following results presented in this chapter, were part of a collaborative effort submitted to the Journal of the Acoustical Society of America(JASA).

5.1 Effect of Frequency

The results of the numerical simulations carried out at different frequencies; 1 MHz ($\lambda \approx 3mm$), $0.5MHz$ ($\lambda \approx 6mm$) and 2 MHz ($\lambda \approx 1.5mm$) are shown in Fig. 5.1,a-c. Gautesen had previously presented the coefficients as a function of wedge angle from 63° to 350°[43, 44]. The present results have been overlayed with Gautesen's results as shown in Fig. 5.1,a-c. Overall, the results seem to agree well when $\theta > 180°$. The largest difference in Tc can be observed when $\theta < 180°$; $\approx 113\%$ at a wedge angle of 80° as shown in Fig. 5.1,a. Rc results presented in Fig. 5.1,b show good agreement at lower wedge angles. P_s values as a function of wedge angle are plotted in Fig. 5.1,c. Similarly, compared to Tc and Rc in Fig. 5.1a-b, the present results agree well with Gautesen's results at wedge angles $\theta > 180°$.

It can be observed that the coefficients also show a dependence on frequency. The Tc at $2MHz$ agrees well with Gautesen's results for a wider range of wedge angles rather than just $\theta > 180°$. The Rc and Ps at 2MHz also match with Gautesen's results. The largest difference can be observed at $0.5MHz$, which does not seem to match Gautesen's results. These results confirm the hypothesis that the coefficients have a frequency dependence.

5.2 Effect of Wedge Angle on Phase

This work extracts the time-amplitude data at different points along the angled boundary depending on the wedge angle. This was done to minimize any such overlap or superposition. This method will essentially give a different phase value depending on the separation between the source and the receiving nodes, which makes it impossible to study the effect on phase. Since the phase will be proportional to the time of flight (TOF), the total travel time can be calculated and correlated with the numerical TOF. The expected TOF from a nodal position before and after the wedge point interaction can be calculated using $t_x = D_x/V_x$; where D_x is the nodal position in mm relative to the input signal location along the boundaries, and V_x is the Rayleigh wave velocity[62, 63] for a given material. Numerical TOF was extracted by performing a Hilbert transform[64] on the time-amplitude data shown in Fig. 2.2,a-b by a red dotted line. From the Hilbert data, the time corresponding to the maximum amplitude was collected at the receiver positions, and the time difference between them was calculated using

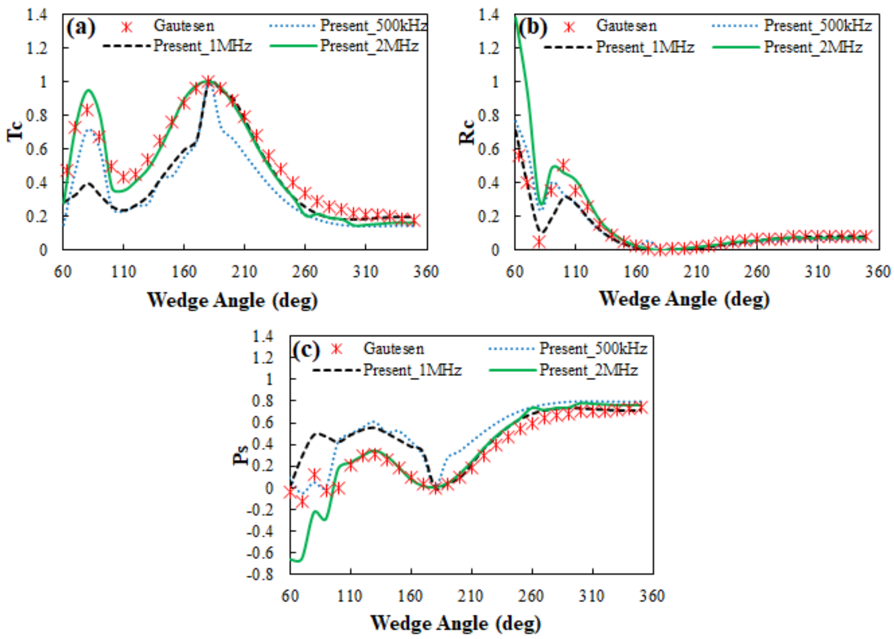

Figure 5.1: Comparing present work at 0.5, 1, 2MHz and Gautesen's model[43, 44]: (a) Tc vs Wedge Angle. (b) Rc vs Wedge Angle. (c) Ps vs Wedge Angle.

$\Delta T_x = t_2 - t_1$.

$$\%Diff = \frac{\Delta T_1 - \Delta T_2}{\Delta T_2} \tag{5.1}$$

Fig. 5.2,a-c shows the difference between numerical vs expected TOF as a function of wedge angle for $0.5MHz$, $1MHz$, and $2MHz$. Fig. 5.2,a at $0.5MHz$ shows that for wedge angles $\theta < 180°$, ΔT is observed to have small fluctuations. At angles $\theta > 180°$, ΔT is observed to have a duality in value. By increasing the excitation frequency to $1MHz$ and $2MHz$ for a wedge angle of 60° to 350°, the fluctuations for ΔT and absolute value in Fig. 5.2,b and c is observed to dissipate.

5.3 Effect of Curvature

To evaluate the effect of the geometry of the discontinuity, a curved geometry as the diffraction source (D2) was modeled as shown in Fig. 5.3. The same material properties described in Sect. 2.1 were used, and $0.5MHz$ was chosen as the excitation frequency. A total of four different wedge angles were modeled and tested with a $\lambda_F = 2.5$ and the resulting radii of curvature values R are shown in Table (5.1). The radius of curvature R was determined by fixing the distance from D1, along both boundaries by a wavelength factor λ_F relative to the excitation frequency used shown in Fig. 5.3 with D2 as the result. A secondary criteria was also used in deciding the radius of curvature R, such that once the λ_F is set, the two end points of the curved section must be tangent with the two connecting straight boundaries denoted with a

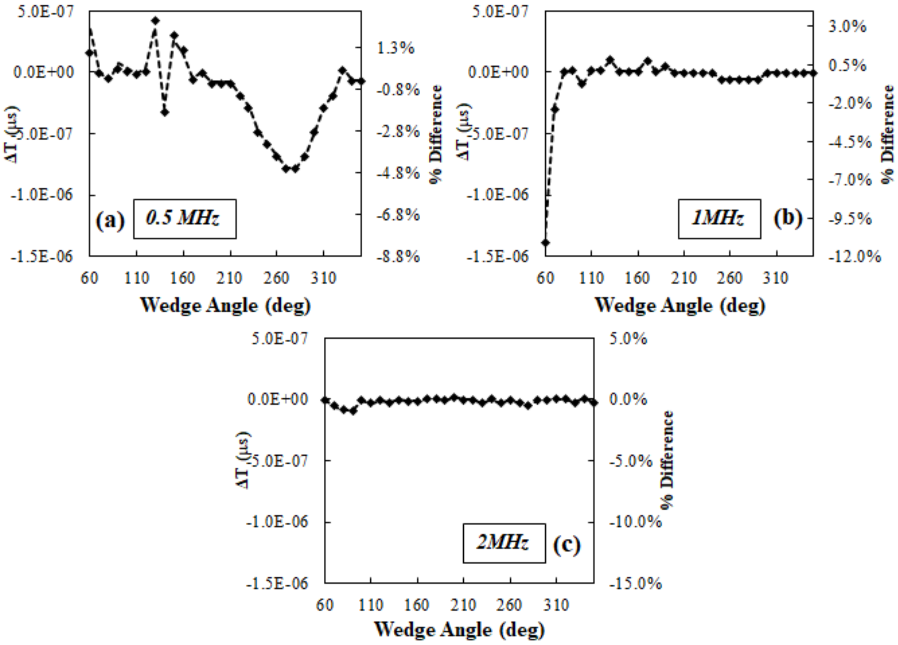

Figure 5.2: Time of Flight: Numerical vs Expected w/ % Difference vs Wedge Angle at (a) 0.5MHz. (b) 1MHz. (c) 2MHz.

light blue dash shown in Fig. 5.3.

Comparing the Tc values in Fig. 5.4,a, it can be observed that the sharp discontinuities have a smaller Tc compared to smoother discontinuity with the exception of 80°. For angles $\theta > 180$, the difference between sharp vs. smooth geometry is smaller. The sharp geometries have higher Rc and Ps values as shown in Fig. 5.4,b and c compared to the curved geometry. Finally, comparing the TOF values, with the exception of 80°, the curve geometry shows no change in TOF as a function of the angle. This is naturally not the case for the sharp geometry, which shows up to 5% change in ΔT as a function of wedge angle.

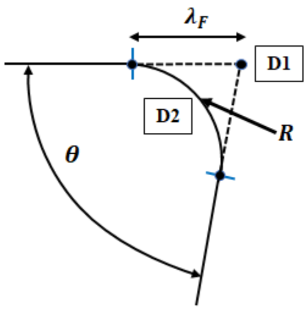

Figure 5.3: Schematic of Curved Wedge Model at 0.5MHz.

5.4 Discussion

Superposition of waves: One of the reasons for the difference between Gautesen's results and the present results could be due to the superposition of the waves. When extracting displacements numerically, the position of the receiver node was chosen such that a single Rayleigh wave

Table 5.1: Radius of Curvature for different wedge angles at $\lambda_F = 2.5$.

Wedge Angle (deg)	Radius of Curvature R (mm)
80	12.59
130	32.17
220	41.21
300	8.66

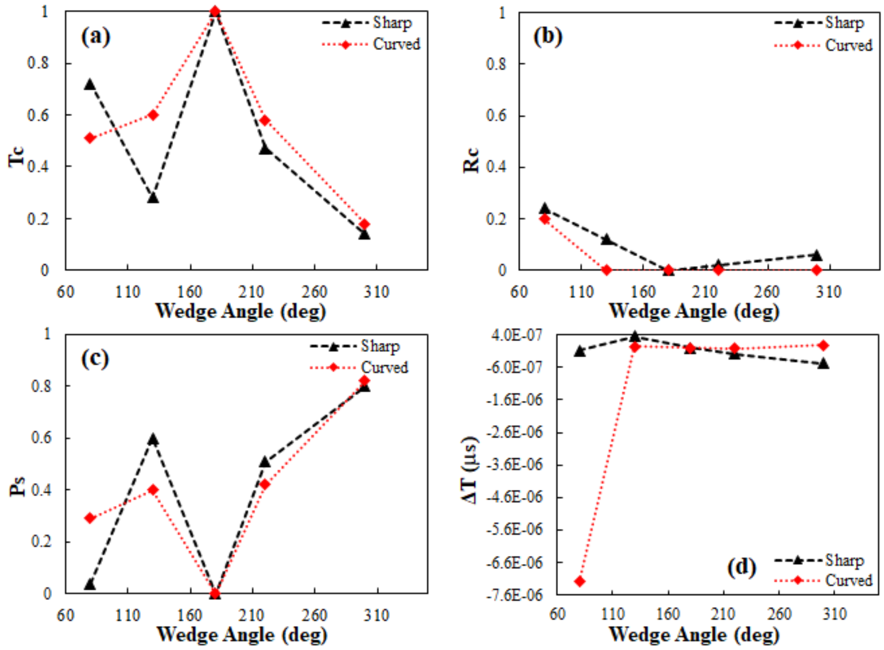

Figure 5.4: Sharp vs Curved Diffraction Source at 0.5MHz (a) Tc vs Wedge Angle. (b) Rc vs Wedge Angle. (c) Ps vs Wedge Angle. (d) Time of Flight (ΔT) vs Wedge Angle.

packet without superposition or interference can be extracted. The local interference between multiple waves after the discontinuity at different time steps is shown in Fig. 5.5,a and b. The vector plots were obtained by extracting the displacement vectors at a given time instance for the entire half-space. As observed in Fig. 5.5,a after interaction the compression(P), shear(SV) and Rayleigh(R) wave modes have not fully separated into clear packets, which is called "undeveloped". In Fig. 5.5,b the transmitted Rayleigh(R_t), reflected Rayleigh(R_r), and shear(SV) wave modes have clearly separated, which is called "fully-developed". By following this criteria of the transmitted wave being undeveloped vs fully-developed, Table (5.2) compares the difference in Tc between the two conditions and Gautesen's results for a 110° wedge angle. It can be observed that the undeveloped wave Tc approximately matches with Gautesen's results, compared to the fully developed wave. The present results suggest that the "undeveloped" wave could possibly be the reason behind the discrepancy for the Tc, Rc values. However, this is valid only at 1MHz or lower and at 2MHz; the Tc values seem to match well with Gautensen's work. This increase in wavelength with decreasing frequency could possibly result in higher superposition. But while extracting displacements, only the fully-developed, discrete wave packets were used for the analysis.

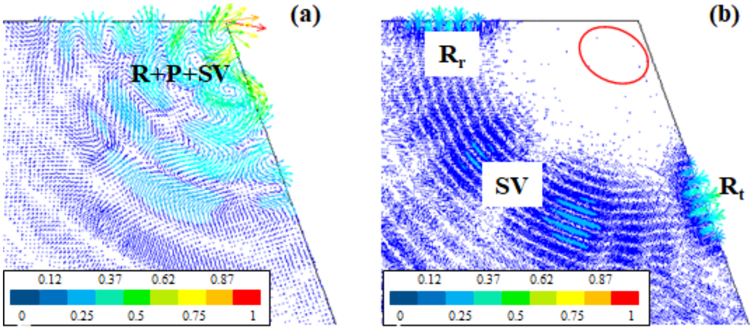

Figure 5.5: Vector Plots for a 110° wedge showing the incident wave packet after D1 interaction (a) Undeveloped wave packet. (b) Fully-developed wave packet.

Table 5.2: Tc at a 110° Wedge comparing an undeveloped wave, fully-developed wave, and previous results.

110° Wedge	Time(s)	Amp(m)	Tc
Undeveloped	$3.1E-5$	$1.659E-6$	0.39
Fully Developed	$3.94E-5$	$1.01E-6$	0.24
Gautesen	-	-	0.435

Effect of frequency: From the results shown in Sect. 5.1, it can be observed that there is a frequency dependence on the coefficients at certain wedge angles with the largest excitation frequency being $2MHz$. The reason for this can be seen from a FE perspective: the larger the excitation frequency, the smaller the Rayleigh wavelength. Based on the convergence criteria stated in Sect. 2.1, if the Rayleigh wavelength decreases, it will increase the amount of elements that are required in a mesh and it becomes very difficult to create a mesh that small. For $\theta > 180°$, there seems to be no dependence on the frequency, and the Tc values seem to follow closely as observed in Fig. 5.1,a. For $100° < \theta < 180°$, the 0.5MHz and 1MHz results match closely, and the 2MHz results match with Gautesen's results. The Tc values in Fig. 5.1,a between $100° < \theta < 180°$ have been plotted as a function of the excitation frequency in Fig. 5.6. The absolute Tc values as a function of angle and frequency were extracted and fitted with different functions. For the Tc vs. θ, a power law fit had the best coefficient of determination (R^2), and a quadratic dependence was observed; $Tc \propto \theta^2$. To determine a functional relationship between Tc and frequency, the data in Fig. 5.6 were fitted with an exponential function, which was once again found to have the highest R^2 value. The frequency dependence was determined to be $Tc(f) \propto e^{f/3}$.

For $60° < \theta < 90°$ the Tc follows a weak parabolic dependence with frequency but does not show any clear dependence. This could be due to the strong interaction of the Rayleigh wave between the two half-space surfaces.

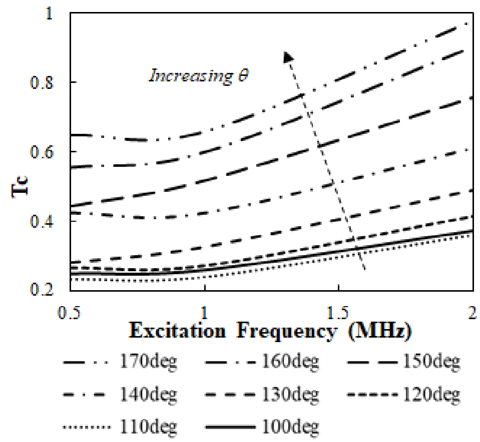

Figure 5.6: Tc vs Excitation Frequency for a 100° to 170° angled wedge.

Phase term: To understand the change in the arrival times for the transmitted wave mode, it is important to understand the phase of the wave modes with a varying angled wedge. As stated in Sect. 1.2 for the analytical models, as the wedge angle decreases, the number of reflected wave modes increases[31, 33, 41, 43, 44]. This can cause multi-mode interactions between the transmitted Rayleigh and the re-reflected wave modes. In any case they could either be in constructive or destructive interference with each other. From the initial excitation frequency of $1MHz$, the change in time of flights(ΔT) does not seem to be affected as much for wedge angles ranging from 180° to 350°. This is contrary to the trend observed in Sect. 5.1 for the change in excitation frequency on the coefficients. The change in excitation frequency for the TOF in Fig. 5.2 does not experience the same linear relationship.

Geometry of the discontinuity: The influence of the type of discontinuity on the Rayleigh wave interaction can be observed in Fig. 5.4,a-c. The sharp transition can act as a single diffraction source resulting in higher scattering. This is evident in the increase Rc and Ps values for the sharp geometry vs. smooth geometry. The Rc and Ps values follow an inverse trend compared to Tc, which is consistent with the hypothesis of higher scattering from sharp discontinuity. However, at 80° and 300° this observation is not true, with the curved geometry having a higher Ps value.

To further analyze this qualitatively, displacement vector plots were extracted for different wedge angles as shown in Fig. 5.7,a-h. The mode conversion of an incident Rayleigh wave into bulk modes (L, S), and the diffraction of the bulk modes is well captured in the vector plots. It is interesting to note that in all the sharp discontinuity (D1) plots, the directivity of the bulk modes, specifically the shear waves are stronger than the curved case. The reflected bulk and Rayleigh modes are also higher in magnitude in the case of D1. Interestingly, there seems to be an angle dependence as well. For example, in the case of $\theta < 90°$ and $\theta > 270°$, the diffraction of the bulk waves seems greater for the curved geometry than the sharp geometry. It can be hypothesized that since the wave is propagating from left to right towards the discontinuity, at certain angles the mode conversion of incident Rayleigh waves into bulk modes will be based on the curvature. Mode conversion of Rayleigh waves into bulk modes has been explored extensively by several authors[25, 65, 66]. The geometry of the wedge can be approximated to a semi-infinite crack when $\theta \rightarrow 360$. Previous studies show that incident Rayleigh waves will diffract into bulk modes with a strong shear window. The curved defect can be approximated into a series of step discontinuities. This will result in each point along the curvature acting like a diffraction source, unlike the sharp discontinuity, where only D1 acts as a discontinuity. As can be noticed in Fig. 5.7,a,b g,h, when the Pointing vector of the scattered mode is opposite to the incident mode, i.e, backward propagating waves[25], (not be confused with reflected waves), the curvature seems to scatter/diffract bulk modes along the entire curve. This is evident in the shear window being much broader for the curved geometry as opposed to the sharp geometry. On the contrary, when the pointing vector is aligned with the incident angle as shown in Fig. 5.7,c,d e,f the overall scatter from the discontinuity is less, and the shear window is smaller as well. This qualitatively agrees with our hypothesis of the effect of the curved geometry. Unfortunately, it is challenging to do a comprehensive quantitative analysis. To establish a quantitative relationship between curvature radius, wedge angle, and Tc can be tedious due to the number of combinations that are possible. The objective of this study is simply to show the effect of curvature on the mode conversion and scattering. An analytical model that can capture these effects would be a more workable solution compared to numerical analysis, which are more suited to capturing the full physics. Secondly, the scatter coefficient can be evaluated from the full scatter field. However, capturing the discrete models as a function of time as performed earlier by Chakrapani[25], is not possible due to the number of overlapping modes. The superposition of the modes makes it impossible to calculate the power flux of the scattered modes.

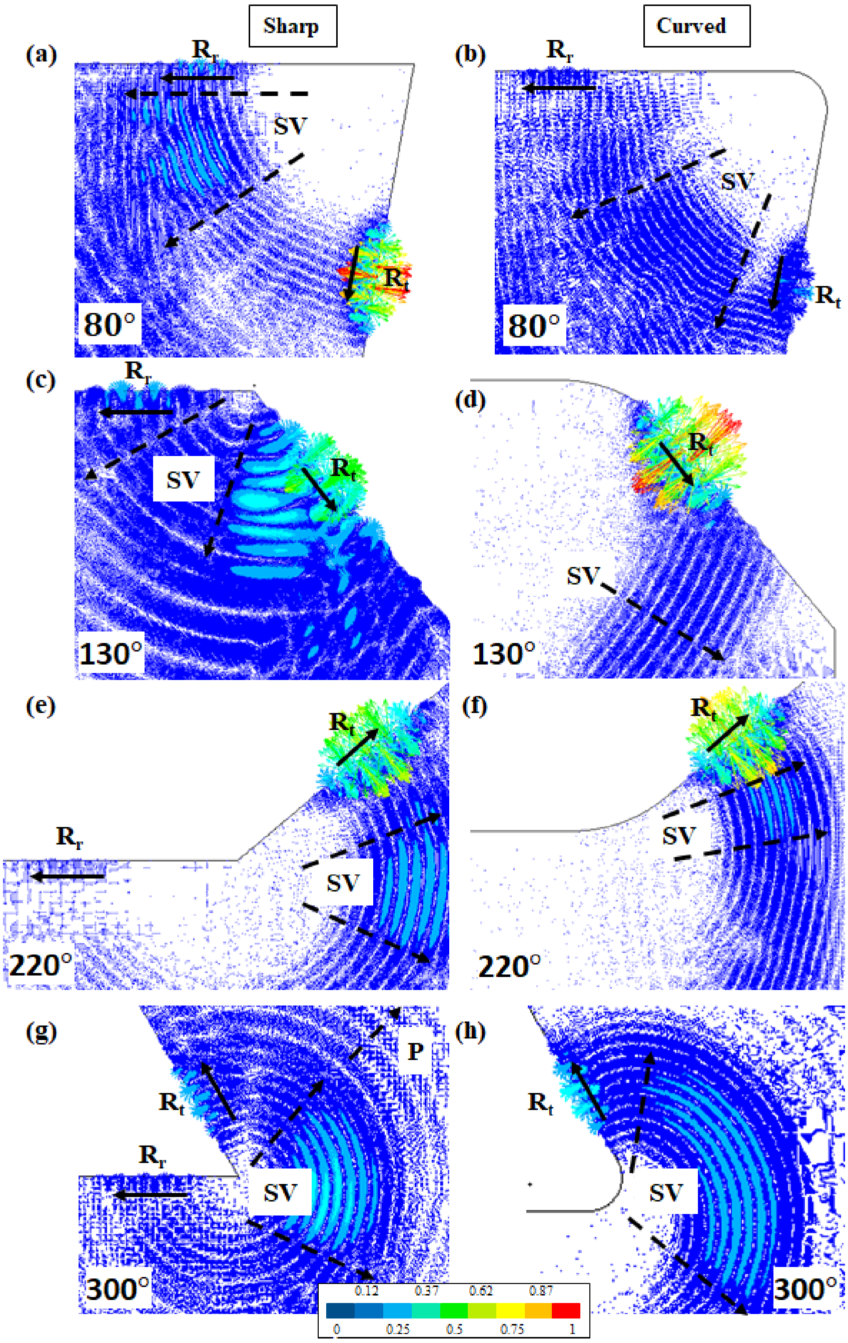

Figure 5.7: Vector plot of incident Rayleigh wave after the discontinuity D1 and D2 interaction: (a) 80° sharp wedge. (b) 80° curved wedge. (c) 130° sharp wedge. (d) 130° curved wedge. (e) 220° sharp wedge. (f) 220° curved wedge. (g) 300° sharp wedge. (h) 300° curved wedge.

Chapter 6

SUMMARY

The interaction of Rayleigh waves with surface breaking RCF/RCD type of defects has been studied using a numerical model. The interaction was characterized using the transmission coefficient of Rayleigh waves. Vertical defects display an asymptotic trend in Tc as the normalized depth increases past 0.67. The oblique defects exhibit a symmetric and sinusoidal Tc response at shallower defect depths between but slowly dissipates as the depth increases. The branched cracks are more complicated and exhibit duality in Tc values. This results in the same Tc value for different branch lengths and orientation combinations.

In order to gain a deeper understanding of the branched crack results, the classical problem of surface/Rayleigh wave interaction with different wedge angles has been revisited. The results from the literature have been compared with the presented studies using numerical methods. The mode conversion and interaction phenomena has been explored by quantifying three main parameters: Tc, Rc, and Ps. In total, three excitation frequencies have been explored with changing wedge angle for Tc, Rc, and Ps; and based on the analysis, the following relationships could be observed for Tc: $Tc \propto e^{f/3}\theta^2$, where f is the excitation frequency and θ is the wedge angle. It was also shown that when the excitation frequency increases, the higher agreement there is with the literature results for different wedge angles. Although, when comparing the presented work and literature results, the superposition of wave modes after interaction with D1 and changing excitation frequencies has been shown to affect the coefficients and TOF with a changing wedge angle, where an extracted Rayleigh mode being "undeveloped" or "fully-developed" as a possible reason for the discrepancies in the coefficients. By introducing a curved transition D2, it was shown to have adverse effects on the coefficients at certain wedge angles opposed to a sharp transition D1. It was also shown to have effects on the Rayleigh to bulk mode conversion where the size of the shear window changes with a transition of D1 to D2.

The cluster defects for Tc and Rc, when represented as a function of defect depth and the number of defects displays both an asymptotic trend and a duality when increasing the depth and the number of defects. These results highlight the complexity of using just the transmission coefficient for characterizing RCF defects. To fully characterize these complex defects, a more data driven approach through signal processing methods might be required but will be explored elsewhere.

The impact of this work is to use the results from the numerical simulations and the signal processing to provide a proof of concept that it can be replicated through experiments and eventually implemented into the field. With all the results then gathered from the experiments, they can be coupled with the numerical works to develop a calibration tool for accurately detecting and characterizing RCF/RCD type of defects for the rail industry. Although being able to determine the exact geometry of the defects can be very difficult, the calibration tool will be used to provide an accurate approximation for some of the defect properties such as depth, incident angle, type, etc.

BIBLIOGRAPHY

[1] A. Poudel and M. Witte. Measuring rolling contact damage in rails using emfi. AAR/MxV Rail Technology Digest. https://aar.com/TD-eLibrary/, 2018. TD18-016.

[2] A. Poudel, M. Witte, P. Gies, and D. Skow. Rolling contact damage characterization on railroad rails using electromagnetic field imaging (emfi). *Materials Evaluation*, 77(7), 2019.

[3] H.M. Tournay. Overview of rolling contact fatigue prediction models. AAR/MxV Rail Technology Digest. https://aar.com/TD-eLibrary/, 2010. TD-10-040.

[4] M.A. Anis, J.P. Srivastava, N.R. Duhan, and P.K. Sarkar. Rolling contact fatigue and wear in rail steels: An overview. In *IOP Conference Series: Materials Science and Engineering*, volume 377, page 012098. IOP Publishing, 2018.

[5] D.F. Cannon, K.O Edel, S.L. Grassie, and K. Sawley. Rail defects: an overview. *Fatigue & Fracture of Engineering Materials & Structures*, 26(10):865–886, 2003.

[6] E.E. et al Magel. *Rolling contact fatigue: a comprehensive review.* United States Department of Transportation. Federal Railroad Administration. Office of Railroad Policy ..., 2011.

[7] A. Kapoor, I. Salehi, and A.M.S. Asih. *Rolling Contact Fatigue (RCF)*, pages 2904–2910. Springer US, Boston, MA, 2013. ISBN 978-0-387-92897-5. doi: 10.1007/978-0-387-92897-5_287. URL https://doi.org/10.1007/978-0-387-92897-5_287.

[8] J. Shen, L. Zhou, H. Rowshandel, G.L. Nicholson, and C.L. Davis. Prediction of rcf clustered cracks dimensions using an acfm sensor and influence of crack length and vertical angle. *Nondestructive Testing and Evaluation*, 35(1):1–18, 2020.

[9] W. Zhong, J.J. Hu, Z.B. Li, Q.Y. Liu, and Z.R. Zhou. A study of rolling contact fatigue crack growth in u75v and u71mn rails. *Wear*, 271(1-2):388–392, 2011.

[10] A. Poudel and M. Witte. Evaluation of in-motion echo-rail rcd measurement system. AAR/MxV Rail Technology Digest. https://aar.com/TD-eLibrary/, 2020. TD 20-007.

[11] A. Poudel and M. Witte. Validation of in-motion echo-rail system for rcd crack depth measurement. AAR/MxV Rail Technology Digest. https://aar.com/TD-eLibrary/, 2021. TD 21-012.

[12] Z. Popović, V. Radović, L. Lazarević, V. Vukadinović, and G. Tepić. Rail inspection of rcf defects. *Metalurgija*, 52(4):537–540, 2013.

[13] W. Fletcher, K. Oldenburg, et al. Transportation statistics annual report 2005. 2005.

[14] S.L. Grassie. Rolling contact fatigue on the british railway system: treatment. *Wear*, 258 (7-8):1310–1318, 2005.

[15] A. Poudel, B. Lindeman, and R. Wilson. Current practices of rail inspection using ultrasonic methods: A review. *Materials Evaluation*, 77(7):870–883, 2019.

[16] D.E. Bray. Detection of flaws in used railroad rail by ultrasonic inspection techniques. *NDT International*, 12(5):217–223, 1979.

[17] T. Heckel, H.M. Thomas, M. Kreutzbruck, and S. Rühe. High speed non-destructive rail testing with advanced ultrasound and eddy-current testing techniques. *NDTIP Proceedings, Prague*, 2009.

[18] S. Alahakoon, Y.Q. Sun, M. Spiryagin, and C. Cole. Rail flaw detection technologies for safer, reliable transportation: a review. *Journal of Dynamic Systems, Measurement, and Control*, 140(2), 2018.

[19] R. Anandika and J. Lundberg. Limitations of eddy current inspection for the characterization of near-surface cracks in railheads. *Proceedings of the Institution of Mechanical Engineers, Part F: Journal of Rail and Rapid Transit*, 236(5):532–544, 2022.

[20] T.A. Alvarenga, A.L. Carvalho, L.M. Honorio, A.S. Cerqueira, L.MA. Filho, and R.A. Nobrega. Detection and classification system for rail surface defects based on eddy current. *Sensors*, 21(23):7937, 2021.

[21] J. Rajamäki, M. Vippola, A. Nurmikolu, and T. Viitala. Limitations of eddy current inspection in railway rail evaluation. *Proceedings of the Institution of Mechanical Engineers, Part F: Journal of Rail and Rapid Transit*, 232(1):121–129, 2018.

[22] J. Zhu, G. Tian, Q. Min, and J. Wu. Comparison study of different features for pocket length quantification of angular defects using eddy current pulsed thermography. *IEEE Transactions on Instrumentation and Measurement*, 68(5):1373–1381, 2019.

[23] E.E. Kriezis, T.D. Tsiboukis, S.M. Panas, and J.A. Tegopoulos. Eddy currents: Theory and applications. *Proceedings of the IEEE*, 80(10):1559–1589, 1992.

[24] S Chakrapani, L Bond, and R Edwards. Rayleigh wave nondestructive evaluation for defect detection and material characterization, 2018.

[25] SK Chakrapani. Numerical study of rayleigh wave propagation along a horizontal semi-infinite crack buried in half-space. *The Journal of the Acoustical Society of America*, 141 (1):137–146, 2017.

[26] R Clark and S Singh. The inspection of thermite welds in railroad rail—a perennial problem. *Insight-Non-Destructive Testing and Condition Monitoring*, 45(6):387–393, 2003.

[27] S. Kenderian, D. Cerniglia, B. Boro Djordjevic, and R.E. Green Jr. Laser-generated acoustic signal interaction with surface flaws on rail wheels. *Research in Nondestructive Evaluation*, 16(4):195–207, 2005.

[28] R.S. Edwards, B. Dutton, M.H. Rosli, and A.R. Clough. Non-contact ultrasonic characterization of angled surface defects. In *AIP Conference Proceedings*, volume 1335, pages 257–264. American Institute of Physics, 2011.

[29] F. Hernandez-Valle, R.S. Edwards, A.R. Clough, M.H. Rosli, and B. Dutton. Laser generation and detection for surface wave interaction with different defect geometries. In *AIP Conference Proceedings*, volume 1511, pages 324–329. American Institute of Physics, 2013.

[30] F. Hernandez-Valle, R.S. Edwards, A.R. Clough, M.H. Rosli, and B. Dutton. Scanning laser techniques for characterisation of different surface breaking defect geometries. In *Proceedings of 18th World Conference on Non-Destructive Testing, Durban, South Africa*, 2012.

[31] AK Mal and L Knopoff. Transmission of rayleigh waves past a step change in elevation. *Bulletin of the seismological society of America*, 55(2):319–334, 1965.

[32] L Knopoff et al. Elastic wave propagation in a wedge. *Wave propagation in solids*, pages 3–43, 1969.

[33] AK Mal and L Knopoff. Transmission of rayleigh waves at a corner. *Bulletin of the seismological society of America*, 56(2):455–466, 1966.

[34] L Knopoff and AF Gangi. Transmission and reflection of rayleigh waves by wedges. *Geophysics*, 25(6):1203–1214, 1960.

[35] AF Gangi. Experimental determination of p wave/rayleigh wave conversion coefficients at a stress-free wedge. *Journal of Geophysical Research*, 72(22):5685–5692, 1967.

[36] BA Auld. Rayleigh wave propagation. In *Rayleigh-Wave Theory and Application*, pages 12–28. Springer, 1985.

[37] H Bateman. Rayleigh waves. *Proceedings of the National Academy of Sciences*, 24(8): 315–320, 1938.

[38] IA Viktorov. Types of acoustic surface waves in solids/review. *Akusticheskii Zhurnal*, 25: 1–17, 1979.

[39] BQ Vu and VK Kinra. Diffraction of rayleigh waves in a half-space. i. normal edge crack. *The Journal of the Acoustical Society of America*, 77(4):1425–1430, 1985.

[40] HL Wong. Effect of surface topography on the diffraction of p, sv, and rayleigh waves. *Bulletin of the Seismological Society of America*, 72(4):1167–1183, 1982.

[41] Bair V Budaev and David B Bogy. Rayleigh wave scattering by a wedge. *Wave Motion*, 22(3):239–257, 1995.

[42] SK Chakrapani, DJ Barnard, and V Dayal. Review of ultrasonic testing for nde of composite wind turbine blades. In *AIP Conference Proceedings*, volume 2102, page 100003. AIP Publishing LLC, 2019.

[43] AK Gautesen. Scattering of a rayleigh wave by an elastic wedge whose angle is less than 180. *Wave Motion*, 36(4):417–424, 2002.

[44] AK Gautesen. Scattering of a rayleigh wave by an elastic wedge whose angle is greater than 180 degrees. *J. Appl. Mech.*, 68(3):476–479, 2001.

[45] AK Gautesen. Scattering of a rayleigh wave by an elastic three-quarter space. *Wave motion*, 35(2):99–106, 2002.

[46] AK Gautesen. Scattering of a rayleigh wave by an elastic quarter space—revisited. *Wave Motion*, 35(1):91–98, 2002.

[47] AK Gautesen. Scattering of a rayleigh wave by an elastic wedge. *Wave Motion*, 9(1):51–59, 1987.

[48] K Fujii. Rayleigh-wave scattering at various wedge corners: investigation in the wider range of wedge angles. *Bulletin of the Seismological Society of America*, 84(6):1916–1924, 1994.

[49] K Fujii, S Takeuchi, Y Okano, and M Nakano. Rayleigh wave scattering at various wedge corners. *Bulletin of the Seismological Society of America*, 74(1):41–60, 1984.

[50] FC Karal Jr and SN Karp. The elastic-field behavior in the neighborhood of a crack of arbitrary angle. *Communications on Pure and Applied Mathematics*, 15(4):413–421, 1962.

[51] FJ Sánchez-Sesma and M Campillo. Topographic effects for incident p, sv and rayleigh waves. *Tectonophysics*, 218(1-3):113–125, 1993.

[52] N Pan, Z Su, L Ye, L-M Zhou, and Y Lu. A quantitative identification approach for delamination in laminated composite beams using digital damage fingerprints (ddfs). *Composite structures*, 75(1-4):559–570, 2006.

[53] F Song, GL Huang, and K Hudson. Guided wave propagation in honeycomb sandwich structures using a piezoelectric actuator/sensor system. *Smart Materials and Structures*, 18(12):125007, 2009.

[54] C Ramadas, K Balasubramaniam, M Joshi, and CV Krishnamurthy. Interaction of the primary anti-symmetric lamb mode (ao) with symmetric delaminations: numerical and experimental studies. *Smart Materials and Structures*, 18(8):085011, 2009.

[55] BA Auld. *Acoustic fields and waves in solids.* , 1973.

[56] X. Jian, S. Dixon, N. Guo, and R.S. Edwards. Rayleigh wave interaction with surface-breaking cracks. *Journal of Applied physics*, 101(6):064906, 2007.

[57] A. Vu, Y. Madhuranthakam, and S.K. Chakrapani. Detection and characterization of rolling contact fatigue type of defects using rayleigh surface waves. In *30th ASNT Research Symposium Conference Proceedings*, volume 30, pages 84–87. American Society for Nondestructive Testing, 2022.

[58] V.K. Kinra and B.Q. Vu. Diffraction of rayleigh waves in a half-space. ii. inclined edge crack. *The Journal of the Acoustical Society of America*, 79(6):1688–1692, 1986.

[59] W. Wang, Z. Zhong, and Y.D. Pan. Scattered echoes from surface defect in the far field of rayleigh wave generated by laser. In *AIP Conference Proceedings*, volume 1650, pages 1307–1315. American Institute of Physics, 2015.

[60] C. Wang, A. Sun, M. Xue, B.F. Ju, J. Xiong, and X. Xu. Width gauging of surface slot using laser-generated rayleigh waves. *Optics & Laser Technology*, 92:15–18, 2017.

[61] M. Ahmad, Z. Liu, A. Basit, W. Bin, and C. He. Characterization of surface crack width in plates using rayleigh wave electromagnetic acoustic transducers. In *IOP Conference Series: Materials Science and Engineering*, volume 1043, page 042038. IOP Publishing, 2021.

[62] LW Schmerr. *Fundamentals of ultrasonic nondestructive evaluation*, volume 122. Springer, 2016.

[63] L.J. Bond S.K. Chakrapani and R.S. Edwards. Rayleigh wave nondestructive evaluation for defect detection and material characterization. *ASM Handbook, Nondestructive Evaluation of Materials*, 17:266–282, 2018.

[64] TJ Ulrich. Envelope calculation from the hilbert transform. *Los Alamos Nat. Lab., Los Alamos, NM, USA, Tech. Rep*, 2006.

[65] N Saffari and LJ Bond. Body to rayleigh wave mode-conversion at steps and slots. *Journal of Nondestructive Evaluation*, 6(1):1–22, 1987.

[66] CP Chang and HS Tuan. On the surface-to-bulk mode conversion of rayleigh waves. *IEEE Transactions on Microwave Theory and Techniques*, 21:558–560, 1973.